Worst-case disturbances for Time-Varying systems

with application to flexible aircraft

Andrea Iannelli[a]
University of Bristol, BS8 1TR, UK

Peter Seiler[b]
University of Minnesota, Minneapolis, MN 55455

Andrés Marcos[c]
University of Bristol, BS8 1TR, UK

The aim of this paper is to propose a method for constructing worst-case disturbances to analyze the performance of Linear Time-Varying systems on a finite time horizon. This is primarily motivated by the goal to analyze flexible aircraft which are more realistically described as time-varying systems, but the same framework can be applied to other fields where this feature is relevant. The performance is defined by means of a generic quadratic cost function, and the main result consists of a numerical algorithm to compute the worst-case signal verifying that a given performance objective is not achieved. The developed algorithm employs the solution to a Riccati differential equation associated with the cost function. Theoretically, the signal can also be obtained by simulating the related Hamiltonian dynamics, but this does not represent a numerically reliable strategy as commented in the paper. The applicability of the approach is demonstrated with a case study consisting of a flexible aircraft subject to gust during a flight test manoeuvre.

[a] Ph.D. Student, Aerospace Engineering Department, University of Bristol
[b] Associate Professor, Aerospace Engineering and Mechanics Department, University of Minnesota
[c] Senior Lecturer, Aerospace Engineering Department, University of Bristol

Nomenclature

G = Linear Time-Varying system

A, B, C, D = Time-varying state matrices of G

d = Input (or disturbance) signal to G.

T = Finite-horizon length, s

J = Quadratic cost function defining a performance of G on $[0, T]$

Q, S, R, F = Linear Time-Varying matrices defining J

$\bar{d}$ = Worst-case signal for the performance associated with J

Y = Solution to a Riccati Differential Equation

H = Hamiltonian matrix associated with a Riccati Differential Equation

V_1, V_2 = Initial and final speeds of the aircraft manoeuvre

a_{z-tR}, a_{z-CG} = Vertical acceleration at the tip of the right wing and at the aircraft center of gravity

OL, CL = Open-loop and closed-loop plants

w_g, d_g = Spatial and temporal profile of the *1-cosine* gust speed, $\frac{m}{s}$

L_g = Gust length, m

I. Introduction

A major challenge faced by the aeronautical industry is to achieve lightweight aircraft configurations that enable to reduce fuel consumption and operating costs while ensuring a feasible design in terms of safety constraints. One of the drawbacks associated with lightweight aircraft is an increased flexibility which can deteriorate performance and hence limit the flight envelope [1, 2]. It is thus acknowledged the importance of developing new tools to analyze this complex scenario while capturing the essential features of the problem.

It is well known that the properties of an aircraft are function of the flight speed V, e.g. the aerodynamic derivatives used in flight mechanics vary with the square of V. In fact, the flight envelope of an aircraft is typically presented in the form of so-called V-n diagrams showing safe combinations of speeds and load factors. This is accentuated in the case of very flexible aircraft because a change in V, by modifying the magnitude of the aerodynamic forces, determines nonneg-

2

ligible deformations on the structure [3–5]. This has been shown to determine a strong coupling between aerodynamics, deformations, and flight mechanics [6], which must be captured for a realistic description of the mission. For these reasons, aircraft manoeuvres involving a change in speed are inherently time-varying. This property holds true in general, since other properties of the system might change during the manoeuvre (e.g. activation of feedback control only during specific parts of the mission), thus the mathematical description of the aircraft dynamics is more accurately given as a Linear Time-Varying (LTV) system. Therefore, standard analysis approaches applicable to Linear Time Invariant (LTI) systems only will not generally provide accurate results for these time-varying scenarios. For example, a common strategy is to evaluate stability and performance at frozen time instances along the trajectory. However, this is not a rigorous approach and it has been shown to lead to erroneous conclusions [7]. An additional feature to take into account is that aircraft manoeuvres are inherently finite, thus performance should be studied considering finite horizons [8]. Note finally that the LTV description can be seen as a preliminary step towards a nonlinear representation of the system. Indeed, a standard approach in aerospace applications [9] is to linearize nonlinear models around different trim points each corresponding to an LTI system. The schematization of this problem with an LTV representation gathering the family of linearised systems is thus a possible approach to capture some nonlinear features of the original system.

Motivated by the previous discussion, the main technical contribution of this paper is a numerical algorithm to compute worst-case disturbances for LTV systems over finite horizons. The construction builds on known results from the optimal control literature [10], which are reviewed in Section II. Specifically, the paper uses a generalization of the strict bounded real lemma [10, 11] stating an equivalence between a bound on a generic cost function J and the existence of a solution Y to a Riccati Differential Equation (RDE). Examples for the $\mathcal{L}_2$ and $\mathcal{L}_2$-to-Euclidean gains show that generic performance metrics can be specified by properly defining J. The Hamiltonian dynamics associated with the RDE is then used in Section III to derive an analytical expression of the worst-case signal which verifies that a certain performance is not achieved. However, a straightforward implementation of this result features numerical issues due to the need of simulating the Hamiltonian dynamics. This observation leads to the main result of the paper, presented in Section

IV, and consisting of a numerically reliable algorithm to construct the worst-case signal based on the solution of the RDE.

The issues associated with the simulation of the Hamiltonian have been considered in the literature [12, 13], but in this work a different approach is taken which exploits the structure of the worst-case signal and the properties of the solution Y. This paper is also closely related to a recent work [11] where a mathematical framework for finite horizon analysis of uncertain LTV systems was proposed. Robust performance of a nominal LTV system interconnected with an uncertain operator, which may model nonlinearities and dynamic or parametric uncertainty, was studied by leveraging the Integral Quadratic Constraints paradigm.

A second contribution of this paper is the demonstration of the applicability of this finite horizon LTV analysis approach using a realistic aeronautic case study. The aircraft demonstrator designed within the European Horizon 2020 project FLEXOP [14, 15] is considered in Section V. Specifically, the effect of atmospheric gusts on its performance during a notional flight test manoeuvre is studied. Available insights are commented and a comparison of the results with a standard approach used for gust analysis in aircraft design discussed.

It is finally observed that the description of a system as time-varying and finite horizon applies also to other engineering applications, including robotic systems [16] and space vehicles [17], which benefit as well from the proposed analysis framework.

Notation: Let $\mathbb{R}^{n \times m}$ and $\mathbb{S}^n$ denote respectively the sets of n-by-m real matrices and n-by-n real symmetric matrices. Given a vector $w \in \mathbb{R}^n$, $||w||$ indicates the Euclidean norm of w. Given $P \in \mathbb{R}^{n \times n}$, $\rho(P)$ indicates the spectral radius of P, i.e. the largest absolute value of its eigenvalues, whereas $\bar{\sigma}(P)$ denotes the induced 2-norm of P. Given a signal $v : [0, T] \to \mathbb{R}^n$, its finite-horizon $\mathcal{L}_2[0, T]$ norm is defined as $||v||_{2,[0,T]} := \left(\int_0^T v(t)^T v(t) dt \geq 0 \right)^{1/2}$. If $||v||_{2,[0,T]}$ is finite then $v \in \mathcal{L}_2[0, T]$. The finite-horizon $\mathcal{L}_\infty[0, T]$ norm is defined as $||v||_{\infty,[0,T]} := \max_{t \in [0,T]} ||v(t)||$.

II. Finite horizon LTV performance

Consider an LTV system G defined on $[0, T]$

$$\dot{x}(t) = A(t)x(t) + B(t)d(t) \tag{1a}$$

$$e(t) = C(t)x(t) + D(t)d(t) \tag{1b}$$

$x \in \mathbb{R}^{n_x}$ is the state, $d \in \mathbb{R}^{n_d}$ is the input, and $e \in \mathbb{R}^{n_e}$ is the output. Note that the input vector d will also be referred to as disturbance throughout the paper due to the meaning attributed to d in this work. The state matrices $A : [0, T] \to \mathbb{R}^{n_x \times n_x}$, $B : [0, T] \to \mathbb{R}^{n_x \times n_d}$, $C : [0, T] \to \mathbb{R}^{n_e \times n_x}$, and $D : [0, T] \to \mathbb{R}^{n_e \times n_d}$ are piecewise-continuous (bounded) functions of time. The dependence on t of these and other time-varying matrices will be omitted when it is clear from the context for ease of presentation. The state response due to an initial condition $x(t_0) = x_0$ at $t_0 \in [0, T]$ and an input $d \in \mathcal{L}_2[0, T]$ can be expressed using the state transition matrix Ψ as follows [18]:

$$x(t) = \Psi(t, t_0)x_0 + \int_{t_0}^{t} \Psi(t, \tau)B(\tau)d(\tau)d\tau \tag{2}$$

It is assumed throughout that $T < \infty$. Thus $x \in \mathcal{L}_2[0, T]$ for any x_0 and $d \in \mathcal{L}_2[0, T]$ [18]. Moreover, there exists a constant M such that $\|\Psi(t, \tau)\| \leq M$ for all $t, \tau \in [0, T]$, i.e. Ψ is uniformly bounded [18].

A generic quadratic cost is introduced next to unify different finite-horizon LTV performance metrics. Let $Q : [0, T] \to \mathbb{S}^{n_x}$, $R : [0, T] \to \mathbb{S}^{n_d}$, $S : [0, T] \to \mathbb{R}^{n_x \times n_d}$, and $F :\in \mathbb{R}^{n_x \times n_x}$ be given. Q, S, and R are assumed to be piecewise-continuous (bounded) functions. A quadratic cost function $J : \mathcal{L}_2[0, T] \to \mathbb{R}$ is defined by (Q,S,R,F) as follows

$$J(d) := x(T)^T F x(T) + \int_0^T \begin{bmatrix} x(t) \\ d(t) \end{bmatrix}^T \begin{bmatrix} Q(t) & S(t) \\ S(t)^T & R(t) \end{bmatrix} \begin{bmatrix} x(t) \\ d(t) \end{bmatrix} dt \tag{3a}$$

$$\text{subject to: Eq. (1a) with } x(0) = 0 \tag{3b}$$

The choice of (Q,S,R,F) defines the particular performance metrics, and the objective with respect to the cost will be illustrated next.

Two well known performance metrics used later on are shown here to be derived from the above general cost function. First, consider the *finite-horizon induced $\mathcal{L}_2$-gain of G*

$$\|G\|_{2,[0,T]} = \sup \left\{ \frac{\|e\|_{2,[0,T]}}{\|d\|_{2,[0,T]}} \,\middle|\, x(0) = 0, 0 \neq d \in \mathcal{L}_{2,[0,T]} \right\} \tag{4}$$

As noted above, the state matrices are assumed to be bounded and the state transition matrix is uniformly bounded. This can be used to show that the induced $\mathcal{L}_2$ gain is bounded for any fixed horizon $T < \infty$. Consider now a given scalar $\gamma > 0$ and select $Q(t) := C(t)^T C(t)$, $S(t) := C(t)^T D(t)$, $R(t) := D(t)^T D(t) - \gamma^2 I_{n_d}$, and $F := 0$. These choices yield the following quadratic cost

$$J_{2,\gamma}(d) = ||e||^2_{2,[0,T]} - \gamma^2 ||d||^2_{2,[0,T]} \tag{5}$$

Thus $J_{2,\gamma}(d) \leqslant 0 \; \forall d \in \mathcal{L}_2[0,T]$ if and only if $||G||_{2,[0,T]} \leqslant \gamma$, which retrieves the performance metric from (4). In order to guarantee a certain performance metric, the objective is then to prove that the cost (3) is negative for all the possible inputs.

Next, assume $D(T) = 0$. Then the *finite-horizon induced $\mathcal{L}_2$-to-Euclidean gain of G* is

$$||G||_{E,[0,T]} = \sup \left\{ \frac{||e(T)||_2}{||d||_{2,[0,T]}} \; \middle| \; x(0) = 0, 0 \neq d \in \mathcal{L}_{2,[0,T]} \right\} \tag{6}$$

The $\mathcal{L}_2$-to-Euclidean gain depends on the system output e only at the final time T, and can be used, for example, to bound the set of states $x(T)$ reachable by disturbances d of a given norm. The assumption that $D(T) = 0$ ensures this gain is well-defined. This performance metric can also be related to the quadratic cost J as follows. Let $\gamma > 0$ be given and select $Q(t) := 0$, $S(t) := 0$, $R(t) := -\gamma^2 I_{n_d}$, and $F := C(T)^T C(T)$. This yields the following cost function

$$J_{E,\gamma}(d) = ||e(T)||^2_2 - \gamma^2 ||d||^2_{2,[0,T]} \tag{7}$$

Thus $J_{E,\gamma}(d) \leqslant 0 \; \forall d \in \mathcal{L}_2[0,T]$ if and only if $||G||_{E,[0,T]} \leqslant \gamma$, which retrieves the performance metric from (6).

The next theorem states an equivalence between a bound on the quadratic cost J and the existence of a solution to a Riccati Differential Equation (RDE).

Theorem 1. *[10] Let (Q,S,R,F) be given with $R(t) \prec 0$ for all $t \in [0,T]$. The following statements are equivalent:*

1. *There exists a constant $\epsilon > 0$ such that $J(d) \leq -\epsilon ||d||^2_{2,[0,T]} \forall d \in \mathcal{L}_2[0,T]$*

2. *There exists a differentiable function $Y : [0,T] \to \mathbb{S}^n$ such that*

$$\dot{Y} + A^T Y + Y A + Q - (YB + S)R^{-1}(YB + S)^T = 0 \tag{8a}$$

$$Y(T) = F \tag{8b}$$

This result is given as Th. 3.7.4 in [10] for the particular case of J corresponding to the induced $\mathcal{L}_2$ gain. A statement and proof for general (Q,S,R,F) cost functions can be found in [11]. Theorem 1 allows to assess the performance of the finite-horizon LTV system in Eq. (1) using the RDE (8). Specifically, the performance $J(d) \leq -\epsilon ||d||^2_{2,[0,T]}$ is achieved if the associated RDE exists on $[0,T]$ when integrated backward from $Y(T) = F$. Conversely, the performance is not achieved if the RDE solution fails to exist on the interval $[0,T]$.

Bisection is often used in conjunction with this theorem to evaluate upper and lower bounds on the system performance. Specifically, the quadratic cost associated with the induced $\mathcal{L}_2$ gain $J_{2,\gamma}$ depends on the choice of γ. If the RDE solution exists on $[0,T]$ for γ then $||G||_{2,[0,T]} < \gamma$, i.e. γ is a valid upper bound (γ_{UB}). Conversely, if γ is selected too small then the RDE solution will fail to exist on $[0,T]$. This can happen only if $Y(t)$ grows unbounded as $t \to t_0 > 0$ when integrating backward from $Y(T) = 0$. Moreover, if Y fails to exist then, by Theorem 1, for all $\epsilon > 0$ there exists a non-trivial d_ϵ such that

$$J_{2,\gamma}(d_\epsilon) = ||e||^2_{2,[0,T]} - \gamma^2 ||d_\epsilon||^2_{2,[0,T]} > -\epsilon ||d_\epsilon||^2_{2,[0,T]} \tag{9}$$

This implies that $||G||_{2,[0,T]} \geq \gamma$, i.e. γ is a lower bound on the induced $\mathcal{L}_2$ gain (γ_{LB}). Moreover, the inputs d_ϵ provide a validation that the gain is greater than or equal to γ.

III. Construction of worst-case disturbance

A. Background on Hamiltonian dynamics

This section provides background on the Hamiltonian dynamics and readers familiar with finite-horizon, two-point boundary problems can skip it and start with Sec. III B where new results are presented.

A two-point boundary value problem is used in the proof of Theorem 1 [10, 11]. This section briefly reviews a related useful result. First consider the following dynamics on $[0,T]$

$$\begin{bmatrix} \dot{x}^*(t) \\ \dot{\lambda}(t) \end{bmatrix} = H(t) \begin{bmatrix} x^*(t) \\ \lambda(t) \end{bmatrix} \tag{10a}$$

$$H := \begin{bmatrix} A & 0 \\ -Q & -A^T \end{bmatrix} + \begin{bmatrix} -B \\ S \end{bmatrix} R^{-1} \begin{bmatrix} S^T & B^T \end{bmatrix} \tag{10b}$$

The matrix H is the time-varying Hamiltonian associated with the RDE in Eq. (8). Denote with Φ the associated state transition matrix. Then, given any final condition $(x^*(T), \lambda(T))$, the solution to Eq. (10) can be written as

$$\begin{bmatrix} x^*(t) \\ \lambda(t) \end{bmatrix} = \Phi(t, T) \begin{bmatrix} x^*(T) \\ \lambda(T) \end{bmatrix} \tag{11}$$

Next define a generalized quadratic cost function $J^*(d, x_0, t_0)$ by

$$J^*(d, x_0, t_0) := x(T)^T F x(T) + \int_{t_0}^{T} \begin{bmatrix} x(t) \\ d(t) \end{bmatrix}^T \begin{bmatrix} Q(t) & S(t) \\ S(t)^T & R(t) \end{bmatrix} \begin{bmatrix} x(t) \\ d(t) \end{bmatrix} dt \tag{12a}$$

$$\text{subject to: } \dot{x} = Ax + Bd \text{ with } x(t_0) = x_0 \tag{12b}$$

Note that the generalized cost J^* differs from the cost J defined in Eq. (3) in that it allows for a non-zero initial condition x_0 at some time $t_0 \in [0, T]$. The next lemma provides a useful relationship between the generalized cost $J^*(d, x_0, t_0)$ and the solution of the Hamiltonian dynamics.

Lemma 1. *Let (Q,S,R,F) be given and let (x^*, λ) be a solution of Eq. (11) from any boundary condition satisfying $\lambda(T) = Fx^*(T)$. For $t_0 \in [0, T]$, define the signal*

$$\bar{d} := \begin{cases} 0 & t < t_0 \\ -R^{-1}(t)(S(t)^T x^*(t) + B(t)^T \lambda(t)) & t \geq t_0 \end{cases} \tag{13}$$

Then $J^*(\bar{d}, x^*(t_0), t_0) = x^*(t_0)^T \lambda(t_0)$, where

$$\begin{bmatrix} x^*(t_0) \\ \lambda(t_0) \end{bmatrix} = \Phi(t_0, T) \begin{bmatrix} x^*(T) \\ \lambda(T) \end{bmatrix} \tag{14}$$

Proof. Note first that the Hamiltonian dynamics (10) can be re-written using the definition of $\bar{d}$ from (13) as follows

$$\begin{bmatrix} \dot{x}^* \\ \dot{\lambda} \end{bmatrix} = \begin{bmatrix} A & 0 \\ -Q & -A^T \end{bmatrix} \begin{bmatrix} x^* \\ \lambda \end{bmatrix} - \begin{bmatrix} -B \\ S \end{bmatrix} \bar{d} \tag{15}$$

Thus, x^* satisfies the LTV dynamics in (12b) with initial condition $x^*(t_0)$. Next, use the definition of $\bar{d}$ and the Hamiltonian dynamics to show the following relation

$$\begin{bmatrix} x^* \\ \bar{d} \end{bmatrix}^T \begin{bmatrix} Q & S \\ S^T & R \end{bmatrix} \begin{bmatrix} x^* \\ \bar{d} \end{bmatrix} = -x^{*^T}(\dot{\lambda} + A^T \lambda) - (\dot{x}^* - Ax^*)^T \lambda \tag{16a}$$

$$= -\frac{d}{dt}(x^{*^T} \lambda) \tag{16b}$$

8

Use this relation to rewrite the generalized cost as

$$J^*(\bar{d}, x^*(t_0), t_0) = x^*(T)^T F x^*(T) - \int_{t_0}^T \frac{d}{dt}(x^{*^T}(t)\lambda(t))dt \tag{17}$$

Integrate the last term and apply the boundary condition $\lambda(T) = F x^*(T)$ to yield $J^*(\bar{d}, x^*(t_0), t_0) = x^*(t_0)^T \lambda(t_0)$.

$\square$

B. Theoretical construction

According to Theorem 1, if there is no solution to the RDE in Eq. (8), then the performance associated with the quadratic cost J is not verified. The objective of the paper is to derive an input signal which confirms that the defined performance is not achieved.

To this end, let us comment on the instances when a solution Y does not exist. Note that the assumption $R(t) \prec 0$ for all $t \in [0, T]$ ensures R is always invertible and hence the RDE is well-defined. Therefore, the only reason for which there is no solution to the RDE is that Y becomes unbounded at a certain time inside the finite horizon. This is exemplified next with a direct application of Theorem 1. The objective is to show what happens to the solution Y of the RDE when there exists an input signal d for which condition 1 of Theorem 1 is not valid.

Example 1. *Consider the following LTI system*

$$\dot{x} = \begin{bmatrix} -11 & -2.5 \\ 4 & 0 \end{bmatrix} x + \begin{bmatrix} 2 \\ 0 \end{bmatrix} d \tag{18}$$

$$e = \begin{bmatrix} 0 & 1.25 \end{bmatrix} x$$

Bisection was used to compute an upper and lower bound on the induced $\mathcal{L}_2$ gain for this system on the horizon $T = 0.1$ s. This yielded the bounds $\gamma_{UB} = 0.0156$ and $\gamma_{LB} = 0.0155$. As noted above, since we are looking at the induced $\mathcal{L}_2$ gain each iteration of the bisection involves integrating the RDE backward from $Y(T) = 0$. Fig. 1 shows the spectral radius of Y on $[0, T]$ for the solutions corresponding to γ_{LB} (red dashed) and γ_{UB} (blue solid). As expected, the solution for γ_{UB} exists on the entire horizon $[0, T]$. On the contrary the RDE solution associated with γ_{LB} fails to exist on the entire horizon. In fact, it grows unbounded at $t_0 \approx 0.015$ when integrating backward from T.
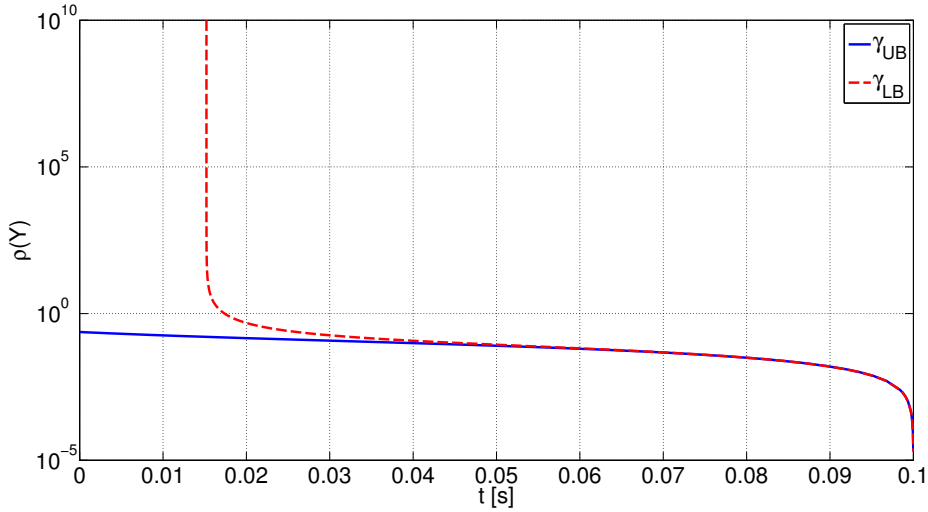
9

Fig. 1 Spectral radius of Y for the upper and lower bound cases.

The main result of this section, prompted by this observation, is reported in the following lemma, which is essentially embedded in the proof of Theorem 1 (equivalently, Theorem 3.7.4 of [10]). It is restated here to highlight the construction of the worst-case disturbance.

Lemma 2. *Let (Q,S,R,F) be given with $R(t) \prec 0$ for all $t \in [0,T]$. Assume the associated RDE in (8) has a solution only in the interval $(t_0, T]$, with $t_0 > 0$. Then there exists a non-trivial input signal $\bar{d} \in \mathcal{L}_2[0,T]$ such that $J(\bar{d}) = 0$.*

Proof. Consider the Hamiltonian dynamics (10) on the horizon $[t_0, T]$ and the associated state transition matrix $\Phi(t, T)$ (11). Next define the matrix functions X_1 and X_2 by

$$\begin{bmatrix} X_1(t,T) \\ X_2(t,T) \end{bmatrix} := \Phi(t,T) \begin{bmatrix} I \\ F \end{bmatrix} = \begin{bmatrix} \Phi_{11}(t,T) & \Phi_{12}(t,T) \\ \Phi_{21}(t,T) & \Phi_{22}(t,T) \end{bmatrix} \begin{bmatrix} I \\ F \end{bmatrix} \tag{19}$$

Here both X_1 and X_2 have n_x rows so that the partitioning is compatible with the states vector $\begin{bmatrix} x^* \\ \lambda \end{bmatrix}$. It can be shown that the RDE solution with boundary condition $Y(T) = F$ satisfies $Y(t) = X_2(t,T)X_1(t,T)^{-1}$ for values of $t \in [0,T]$ where the RDE solution exists [11].

By hypothesis, the RDE cannot be integrated backward from $Y(T) = F$ in the interval $[0,T]$. Specifically, it is assumed that Y only exists in the interval $(t_0, T]$. Note that $\Phi(t,T)$ is uniformly bounded in t and this implies that $X_2(t,T)$ is also uniformly bounded in t. Hence $Y(t)$ becomes unbounded as $t \to t_0$ if and only if $X_1(t_0, T)$ is singular. Thus, there exists a non-trivial vector

v such that $X_1(t_0, T)v = 0$. Setting $x^*(T) = v$ and $\lambda(T) = Fv$, a solution of Eq. (11) can be determined as follows

$$\begin{bmatrix} x^*(t) \\ \lambda(t) \end{bmatrix} = \Phi(t,T) \begin{bmatrix} v \\ Fv \end{bmatrix} = \begin{bmatrix} X_1(t,T) \\ X_2(t,T) \end{bmatrix} v \tag{20}$$

Note that for this solution it holds $x^*(t_0) = X_1(t_0, T)v = 0$.

Construct $\bar{d}$ based on (13) using the solution to the Hamiltonian dynamics given in (20). Apply Lemma 1 to show that $J^*(\bar{d}, 0, t_0) = 0$. Note finally from (15) that the response of the original LTV system (1) with input $\bar{d}$ and initial condition $x(0) = 0$ is given by $x(t) = 0$ for $t < t_0$ and $x(t) = x^*(t)$ for $t \geq t_0$. As a consequence, it holds that $J(\bar{d}) = J^*(\bar{d}, 0, t_0) = 0$, which proves the statement. $\qquad\square$

C. A naive numerical implementation

The proof of Lemma 2 is constructive, in that it suggests a strategy to construct the worst-case disturbance $\bar{d}$ based on the solution (20) of the Hamiltonian dynamics. Next, a pseudocode for a straightforward implementation of the proposed algorithm is provided.

Algorithm 1 Construction of $\bar{d}$ based on simulation of the Hamiltonian dynamics
---
1: **Given**: (Q,S,R,F) such that a solution $Y(t)$ exists for $t \in (t_0, T]$, $t_0 > 0$

2: **Compute** X_1: Calculate the state transition matrix $\Phi(t,T)$ of Eq. (10) and build $X_1(t_0, T) = \Phi_{11}(t_0, T) + \Phi_{12}(t_0, T)F$

3: **Compute** v: Solve the eigenvalue problem for $X_1(t_0, T)$ and determine the eigenvector v associated with the eigenvalue with the smallest magnitude

4: **Compute** (x^*, λ): Use $\Phi(t,T)$ from step 2 and Eq. (20)

5: **Build** $\bar{d}$: Use Eq. (13)

The main issue with Algorithm 1 arises from step 2, which requires computing the state transition matrix of the Hamiltonian dynamics. This is achieved by simulating Eq. (10) for a set of linearly independent boundary conditions at $t = T$ (single-point boundary conditions). However, it is known that for LTI systems and quadratic cost functions the eigenvalues of the constant matrix H are symmetric about the imaginary axis [19]. This will compromise the accuracy in predicting the worst-case signal, since the procedure relies on simulating a system with unstable dynamics.

Example 2. *The induced $\mathcal{L}_2$ gain for the LTI system (18) introduced in Example 1 is studied. A generic finite horizon $[0, T]$ is considered, and the bisection algorithm is first applied to determine guaranteed bounds on the performance objective. As noted previously, the cost function $J_{2,\gamma}$ depends on the value of γ. Algorithm 1 can be used to compute the worst-case disturbance from the cost function matrices (Q, S, R, F) associated with the performance lower bound γ_{LB}. Fig. 2 shows a comparison for different T between γ_{LB} (obtained via bisection using the RDE) and $\gamma_d = \frac{||\bar{e}||_{2,[0,T]}}{||\bar{d}||_{2,[0,T]}}$, where $\bar{e}$ is the output of (18) corresponding to the input signal $\bar{d}$ given by Algorithm 1.*
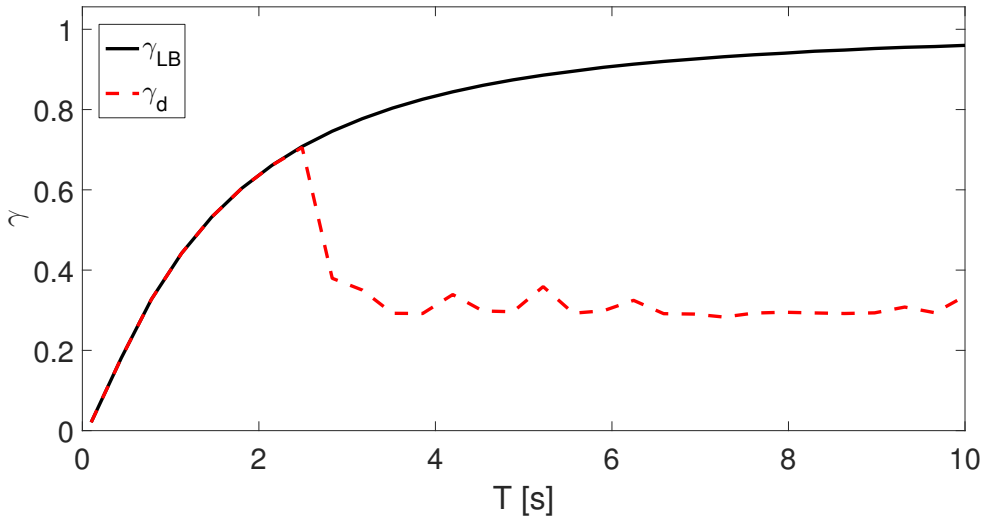

Fig. 2 Worst-case $\mathcal{L}_2$ gain from Algorithm 1 vs. guaranteed γ_{LB} for different horizons T.

It can be noted that when small finite horizons are considered ($T \leq 2s$), the two values are practically the same, that is, Algorithm 1 accurately provides the worst-case signal $\bar{d}$. But as T increases, the gain γ_d is markedly different than the one obtained via bisection. Given that the latter provides a guaranteed lower bound on the metric, it is inferred that the calculation underlying γ_d is incorrect.

This result can be understood by considering the Hamiltonian H associated with Eq. (18), which is time-invariant and whose spectrum, irrespective of the final time T, has always two eigenvalues on the imaginary axis and two on the real axis (symmetric about the imaginary axis). For example, for $T = 10$, the two pairs of eigenvalues are respectively $\pm\ 0.29i\ \frac{rad}{s}$ and $\pm\ 10.05\ \frac{rad}{s}$. As the finite horizon increases, the integration of the associated dynamics (step 2 of Algorithm 1) is performed on a larger time window. Thus the accuracy in computing the state transition matrix deteriorates

due to the unstable dynamics. Consequently, $X_1(t_0, T)$ and its eigenvector v (step 3) are also poorly estimated, and this explains why the worst-case disturbance is not well captured.

IV. An improved construction of worst-case disturbance

The main technical contribution of the paper is presented in this section. It consists of an algorithm to compute $\bar{d}$ which avoids numerical integration of the Hamiltonian dynamics (10). The main idea is to exploit the solution Y of the RDE to construct the worst-case signal. The following lemma is similar to Lemma 2 but the proof allows for an alternative construction for the disturbance that does not entail simulating H.

Lemma 3. *Let (Q,S,R,F) be given with $R(t) \prec 0$ for all $t \in [0, T]$. Assume the associated RDE in (8) has a solution only in the interval $(t_0, T]$, with $t_0 > 0$. Then for all $\epsilon > 0$ there exists a non-trivial disturbance $\bar{d}_\epsilon$ such that $J(\bar{d}_\epsilon) > -\epsilon ||\bar{d}_\epsilon||^2_{2,[0,T]}$, i.e. condition 1 in Theorem 1 fails to hold.*

Proof. By hypothesis, the solution $Y(\hat{t}_0)$ to the RDE exists for any $\hat{t}_0$ in $(t_0, T]$. Let (w, g) denote the eigenpair of $Y(\hat{t}_0)$ associated with its largest eigenvalue in magnitude, i.e. $Y(\hat{t}_0)w = gw$, $g = \rho(Y(\hat{t}_0))$, and $||w|| = 1$. It holds that $\rho(Y(\hat{t}_0)) \to \infty$ as $\hat{t}_0 \to t_0$ (as discussed in the proof of Lemma 2 and Example 1).

Next, recall the definition for (X_1, X_2) given in Eq. (19) and that $Y(t) = X_2(t, T)X_1(t, T)^{-1}$ for values of t where Y exists. Let x^* and λ be the solution of the Hamiltonian dynamics with the following boundary condition

$$\begin{bmatrix} x^*(T) \\ \lambda(T) \end{bmatrix} = \begin{bmatrix} I \\ F \end{bmatrix} z; \quad \text{where} \ \ z := X_1(\hat{t}_0, T)^{-1}\frac{w}{g} \tag{21}$$

Then it is possible to construct $\bar{d}$ as in (13) using the solution (x^*, λ) and $t_0 = \hat{t}_0$ Without loss of generality $\bar{d}$ is scaled such that $||\bar{d}||^2_{2,[0,T]} = 1$. Note that the signal $\bar{d}$ depends on the choice of $\hat{t}_0$ due to the boundary conditions in (21), i.e. $\bar{d} = \bar{d}_{\hat{t}_0}$. The subscript $\hat{t}_0$ will be omitted in the sequel for clarity.

The solution of the Hamiltonian dynamics at $t = \hat{t}_0$ is given by

$$\begin{bmatrix} x^*(\hat{t}_0) \\ \lambda(\hat{t}_0) \end{bmatrix} = \begin{bmatrix} X_1(\hat{t}_0, T) \\ X_2(\hat{t}_0, T) \end{bmatrix} z = \begin{bmatrix} I \\ Y(\hat{t}_0) \end{bmatrix} \frac{w}{g} = \begin{bmatrix} \frac{w}{g} \\ w \end{bmatrix} \tag{22}$$

It follows from Lemma 1 that $J^*(\bar{d}, x^*(\hat{t}_0), \hat{t}_0) = \frac{w^T w}{g}$. It is important to note, however, that $J^*(\bar{d}, x^*(\hat{t}_0), \hat{t}_0) \neq J(\bar{d})$ due to the non-zero initial conditions. Specifically, the solution of the Hamiltonian dynamics satisfies the following on $[\hat{t}_0, T]$

$$\dot{x}^* = Ax^* + B\bar{d} \quad \text{with} \quad x^*(\hat{t}_0) = \frac{w}{g} \tag{23}$$

However, applying $\bar{d}$ to the original LTV system (1a) from $x(0) = 0$ yields $x(t) = 0$ on $[0, \hat{t}_0)$ and the following dynamics on $[\hat{t}_0, T]$

$$\dot{x} = Ax + B\bar{d} \quad \text{with} \quad x(\hat{t}_0) = 0 \tag{24}$$

To complete the proof, first rewrite $J(\bar{d})$

$$\begin{aligned} J(\bar{d}) =& x(T)^T F x(T) + \int_{\hat{t}_0}^T [\begin{smallmatrix} x \\ d \end{smallmatrix}]^T \begin{bmatrix} Q & S \\ S^T & R \end{bmatrix} [\begin{smallmatrix} x \\ d \end{smallmatrix}] \, dt \\ =& J^*(\bar{d}, x^*(\hat{t}_0), \hat{t}_0) + \chi \\ =& \frac{w^T w}{g} + \chi \end{aligned} \tag{25}$$

where the term χ is given by

$$\chi := x(T)^T F x(T) + \int_{\hat{t}_0}^T [\begin{smallmatrix} x \\ d \end{smallmatrix}]^T \begin{bmatrix} Q & S \\ S^T & R \end{bmatrix} [\begin{smallmatrix} x \\ d \end{smallmatrix}] \, dt - x^*(T)^T F x^*(T) - \int_{\hat{t}_0}^T [\begin{smallmatrix} x^* \\ d \end{smallmatrix}]^T \begin{bmatrix} Q & S \\ S^T & R \end{bmatrix} [\begin{smallmatrix} x^* \\ d \end{smallmatrix}] \, dt \tag{26}$$

Using Lemma 4 in the Appendix, this error term can be bounded as follows

$$|\chi| \leq \left[\bar{\sigma}(F) + (T - \hat{t}_0) \max_{t \in [\hat{t}_0, T]} \bar{\sigma}\left(\begin{bmatrix} Q(t) & S(t) \\ S^T(t) & R(t) \end{bmatrix} \right) \right] \left[||x||_{\infty, [\hat{t}_0, T]} + ||x^*||_{\infty, [\hat{t}_0, T]} \right] ||x - x^*||_{\infty, [\hat{t}_0, T]} \tag{27}$$

Both $||x||_{\infty, [\hat{t}_0, T]}$ and $||x^*||_{\infty, [\hat{t}_0, T]}$ are uniformly bounded as $\hat{t}_0 \to t_0$ because $\bar{d}(=\bar{d}_{\hat{t}_0})$ is selected to satisfy $||\bar{d}||_{2, [0, T]}^2 = 1$. Moreover, $x(t) - x^*(t) = -\Psi(t, \hat{t}_0) \frac{w}{g}$ so that $||x - x^*||_{\infty, [\hat{t}_0, T]} \to 0$ as $\hat{t}_0 \to t_0$. Therefore, it follows that $|\chi| \to 0$ as $\hat{t}_0 \to t_0$.

Finally, it follows from (25) that $|J(\bar{d})| \to 0$ as $\hat{t}_0 \to t_0$. Thus, for all $\epsilon > 0$ there exists a $\hat{t}_0 \in (t_0, T]$ such that $\bar{d}(=\bar{d}_{\hat{t}_0})$ yields $||\bar{d}||_{2, [0, T]} = 1$ and $J(\bar{d}) > -\epsilon$.

$\square$

Lemma 3 is also constructive, because the worst-case disturbance can be obtained by computing x^* and λ with initial conditions (22). However, a straightforward implementation of this would still require the integration of the Hamiltonian H. The task of simulating the states of the Hamiltonian dynamics only without incurring numerical issues have been considered in the literature. For example in [12, 13] a Riccati transformation of the Hamiltonian is proposed (note that this would have not applied to Algorithm 1 which prescribed to compute the state transition matrix of H).

Another approach is taken here, prompted by the observation that if $\begin{bmatrix} x^*(T) \\ \lambda(T) \end{bmatrix} = \begin{bmatrix} I \\ F \end{bmatrix} z$ then

$$\begin{bmatrix} x^*(t) \\ \lambda(t) \end{bmatrix} = \begin{bmatrix} X_1(t,T) \\ X_2(t,T) \end{bmatrix} z = \begin{bmatrix} I \\ Y(t) \end{bmatrix} X_1(t,T)z \tag{28}$$

This means that $\lambda(t) = Y(t)x^*(t)$ for all $t \in [\hat{t}_0, T]$, which allows to express the disturbance $\bar{d}$ equivalently in terms of (x^*, Y) rather than (x^*, λ). Specifically, for $t \in [\hat{t}_0, T]$ it holds

$$\begin{aligned} \bar{d} &= -R^{-1}(S^T x^* + B^T \lambda) \\ &= -R^{-1}(S^T + B^T Y)x^* \end{aligned} \tag{29}$$

The states x^* of the Hamiltonian dynamics are thus given by

$$\dot{x}^* = (A - BR^{-1}(S^T + B^T Y))x^* \tag{30}$$

Eq. (30) can be used now to compute x^* without direct integration of H. Then, the states x^* and RDE solution Y can be used to construct the disturbance according to (29). These formulae implicitly reconstruct the co-states as $\lambda(t) = Y(t)x^*(t)$.

The following pseudocode recaps the main steps of the proposed algorithm to compute the worst-case disturbance without numerical integration of the Hamiltonian dynamics.

Algorithm 2 Construction of $\bar{d}$ exploiting the solution of the RDE

1: **Given:** (Q,S,R,F), the associated RDE solution existing on $(t_0, T]$, and some time $\hat{t}_0 \in (t_0, T]$

2: **Compute** BC: evaluate the eigenpair (g, w) associated with the largest (in magnitude) eigenvalue of $Y(\hat{t}_0)$

3: **Simulate** x^* with Eq. (30) from the initial condition $x^*(\hat{t}_0) = \frac{w}{g}$

4: **Build** $\bar{d}$: Use x^* and Y to construct $\bar{d}$ using Eq. (29)

Note that with this approach only n_x states are simulated (step 3 of Algorithm 2), which leads to a reduction in the run time compared to the calculation of the state transition matrix of H

prescribed by Algorithm 1. More importantly, Algorithm 2 is not subject to the aforementioned numerical issues because the states x^* are not obtained by simulation of the Hamiltonian, but rather by exploiting the knowledge of the solution Y of the RDE. The next example showcases this using the LTI system considered in the previous examples.

Example 3. *The induced $\mathcal{L}_2$ gain for the LTI system introduced in Example 1 is considered again. As done in Example 2, a comparison between γ_{LB} (obtained via bisection) and $\gamma_d = \frac{||\bar{e}||_{2,[0,T]}}{||\bar{d}||_{2,[0,T]}}$ is considered. The difference is that $\bar{e}$ corresponds now to the input signal $\bar{d}$ given by Algorithm 2. Fig. 3 shows that Algorithm 2 is capable of accurately predicting the worst-case signal. Indeed γ_d matches the guaranteed lower bound γ_{LB} for all the finite horizons.*
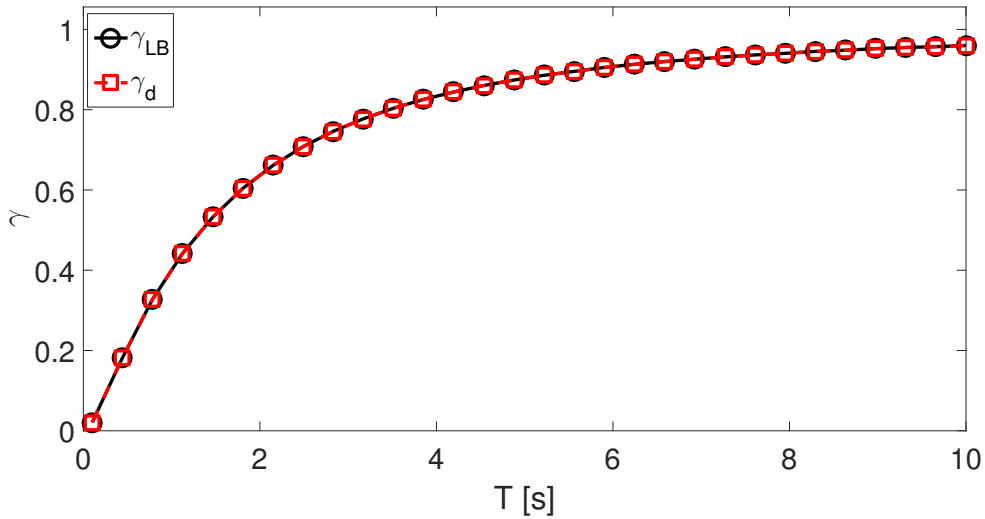

Fig. 3 Worst-case $\mathcal{L}_2$ gain from Algorithm 2 vs. guaranteed γ_{LB} for different horizons T.

Algorithm 2 is implemented in the LTVTools toolbox [20], where the study of nominal and uncertain LTV systems [11] can be efficiently performed.

V.   Analysis of the FLEXOP aircraft

A.   Case study definition

This Section shows an application of the LTV framework developed in the first part of the paper to investigate performance of flexible aircraft. Specifically, the case study consists of the planned flight test scenario that will be considered in the FLEXOP project to validate flutter suppression designs [14]. Flutter is an aeroelastic instability determined by a detrimental interaction between

aerodynamics and elastic forces [21]. As the speed is increased, this coupling becomes stronger until stability is lost. The speed at which this happens is called flutter speed, and it is often a key requirement in the design of an aircraft. One of the goals of the FLEXOP project is to demonstrate the applicability of control design strategies to increase the flutter speed and thus enlarge the safe flight envelope of the aircraft.

Fig. 4 shows a schematic representation of the demonstrator developed by the FLEXOP consortium, where the control effectors and sensors for closed-loop control are highlighted. Specifically, 8 control surfaces, 4 for each wing (R right and L left), are available. As for the sensors, accelerometers at 3 stations across each wing and one in the center of gravity of the aircraft are also indicated with black rectangles. Tab. 1 reports the main design features of the aircraft [15].
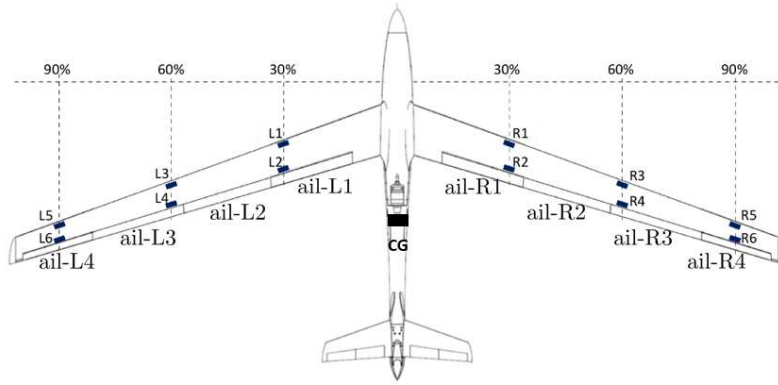

Fig. 4 Schematic view of the FLEXOP demonstrator's control surfaces and sensors.

Table 1 FLEXOP demonstrator design features

Wingspan	$7m$
Aspect ratio	20
Takeoff Mass	55 kg

The scenario considered consists of a uniformly accelerated level flight manoeuvre from a speed V_1 to V_2. The manoeuvre starts at $t = 0$ with an initial speed V_1 and is concluded at $t = T = 2\frac{L_{ac}}{V_1+V_2}$, where L_{ac} denotes the covered distance. In this article it will be considered $V_1 = 45\frac{m}{s}$, $V_2 = 49\frac{m}{s}$, and $L_{ac} = 250m$ (hence $T = 5.3s$).

The aircraft is described by a grid of LTI plants obtained at 5 uniformly spaced points between V_1 and V_2. Each model has 38 states capturing the interaction between rigid body, elastic dynamics, and unsteady aerodynamic. These models, providing the (constant) state-matrices A, B, C, and D at fixed times, were obtained via model reduction from 1000+ states LTI models derived by trimming the high-fidelity nonlinear aeroelastic solver. By assuming an uniformly accelerated manoeuvre, the state-matrices can be linearly interpolated with respect to time in the horizon $[0, T]$. This allows to finally build up the LTV model G_{LTV}, capturing the variability of the aircraft properties in the speed interval $[V_1, V_2]$. Consistently with the generic LTV model defined in Eq. (1), the input and output vectors considered in the analyses will be denoted respectively by d and e. The disturbance d assumed here is a uniform vertical wind gust. Since the models do not have dedicated input channels for gust, this is accounted for by means of the control surface inputs $\delta_{ail-L\bullet}$ and $\delta_{ail-R\bullet}$ (with $\bullet = 1, 2, 3, 4$). The premise for this is that, to a first approximation, the effect of a vertical gust is to change the local angle of attack of the wing, thus it can be captured as an equivalent rotation of the control surfaces (which modify the curvature of the section, hence resulting in a similar effect to a change in the angle of attack). Therefore the input d has the units of speed (i.e. $\frac{m}{s}$). Then, by means of first approximation formulas [22], this is scaled and will finally result in control surfaces rotation units (i.e. rad). When a uniform symmetric gust is considered, the control surfaces have all the same rotation, i.e. $\delta_{ail-L\bullet} = \delta_{ail-R\bullet} = d$, which is the case studied in the paper. This is done here for exemplification, but variations of the wing's sections and gust properties along the span can be easily modelled within this description. As for the outputs e, two different cases will be studied: vertical acceleration at the tip of the right wing a_{z-tR} (specifically, at the sensor R6 depicted in Fig. 4) and at the aircraft center of gravity (CG) a_{z-CG}. In both cases, e is normalized with the gravitational acceleration g. Note finally that, due to the linearity of the problem, the worst-case disturbance can be arbitrarily scaled. For a better representation and comparison of the time-domain responses, the signals shown in the plots are adimensionalized and normalized such that $||d||_{2,[0,T]} = 1$.

The objective of the analyses performed in here is to compute the susceptibility of the demonstrator to gust during a finite-horizon manoeuvre. In particular, the importance of capturing the

time-varying nature of the problem (next subsection) and the difference between open and closed-loop performance (Sec. V C) will be investigated. Finally, a comparison of this approach with traditional gust analyses employed in the aerospace community is proposed in Sec. V D.

B.   Finite horizon LTI vs LTV

In this subsection the importance of considering the time-varying feature of the problem in the assessment of aircraft performance is investigated. The two performance metrics defined in Eqs. (4) and (6) (respectively induced $\mathcal{L}_2$ and $\mathcal{L}_2$-to-Euclidean gains) are analyzed, and the bisection algorithm commented in Sec. II is applied. Tab. 2 reports the results in terms of upper bounds on the performance γ_{UB}. In the first column the adopted model is defined: G_1, G_m, and G_2 are the LTI models at speeds V_1, V_m (mid-speed), and V_2 respectively; and G_{LTV} is the LTV model. In the second and third columns the two performance metrics for a_{z-tR} are listed (fourth and fifth columns for a_{z-CG}). It is emphasized that for both LTI and LTV analyses a finite-horizon problem (of length $T = 5.3s$) is considered.

Table 2 Comparison of finite horizons LTI and LTV performance based on the upper bound of $\mathcal{L}_2$ and Euclidean gains

Model	$\|\|G\|\|_2^{tR}$	$\|\|G\|\|_E^{tR}$	$\|\|G\|\|_2^{CG}$	$\|\|G\|\|_E^{CG}$
G_1	12.7	21.9	1.7	2.1
G_m	18.3	26.1	2.4	2.8
G_2	31.1	34.7	4.3	4.3
G_{LTV}	20	32	2.7	3.8

It can be inferred from the results that analyzing the aircraft manoeuvre with a frozen LTI approach leads to different results than with the LTV framework. A classic approach when adopting the former strategy is to consider the LTI plant corresponding to the mid-speed, on the basis that this sufficiently captures the effect of varying the speed. The results in Tab. 2 show that this is approximately true only for the induced $\mathcal{L}_2$ gain (i.e. columns 2 and 4). In fact, by looking at columns 3 and 5 it can be noted that the predictions obtained with G_{LTV} are closer to the ones with G_2 (i.e. the plant at the final speed). Thus, by only considering a handful of cases, it is already

apparent that none of the LTI models matches the LTV results for all the performance tests.

By comparing the performance for the two outputs (CG and tip accelerations), it is also observed a substantial difference between the values, which can be interpreted as a measure of the flexibility of the wing. Complementing the quantitative information from Tab. 2, it is possible to identify the worst-case signals for both performance metrics. In particular, in Fig. 5 the worst-case signals for the induced $\mathcal{L}_2$ gain of a_{z-CG} obtained with G_m and G_{LTV} are plotted, whereas Fig. 6 shows those corresponding to the Euclidean norm of a_{z-tR}. The cases for G_1 and G_2 are not shown here but have disturbance profiles similar to that of G_m. Recall that d is dimensionless, and scaled such that $||d||_{2,[0,T]} = 1$.
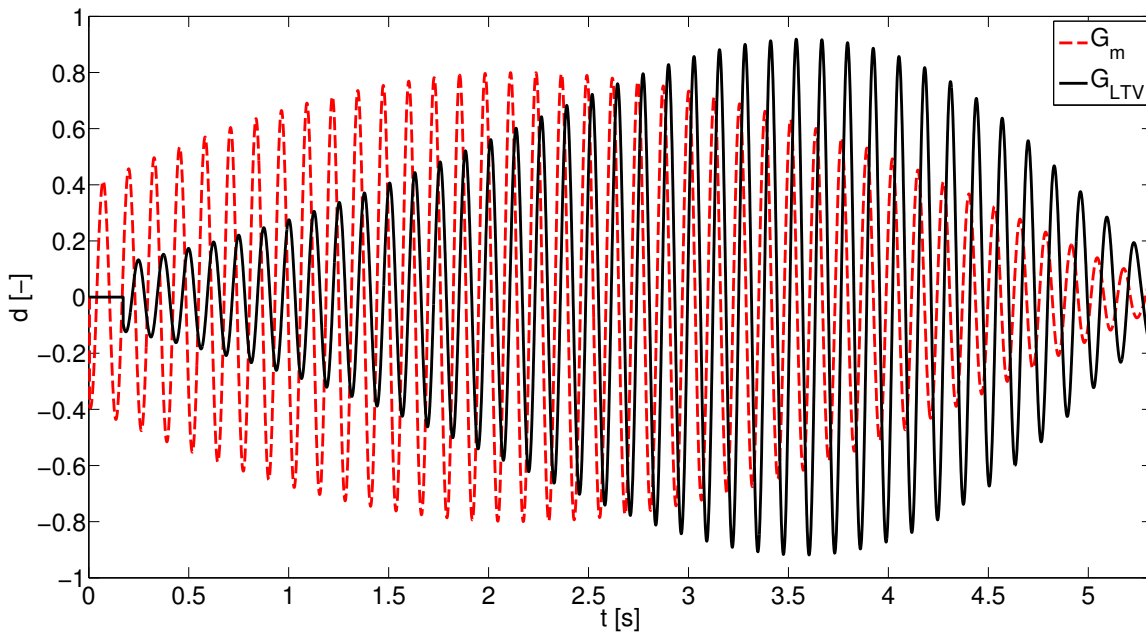

Fig. 5 Comparison between $\mathcal{L}_2$ gain worst-case disturbances for a_{z-CG}.

From the figures it can be seen that the worst-case disturbance corresponding to the LTI system is different from the LTV case. This is more markedly noticeable from Fig. 5, but can also be appreciated in Fig. 6 where the discrepancies in the final part of the input signal have a large effect on the performance (being it dependent on the value of the output at $t = T$ only). Thus, it is confirmed the importance of capturing the time variance of the system, anticipated by Tab. 2, in analysing the considered manoeuvre.
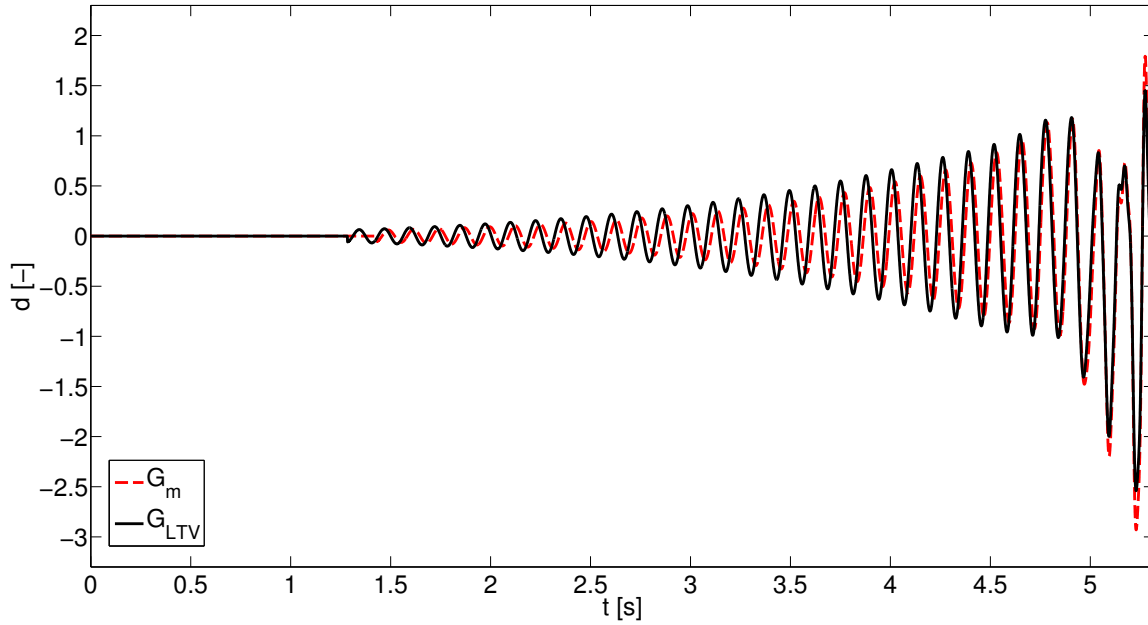
Fig. 6 Comparison between Euclidean gain worst-case disturbances for a_{z-tR}.

C. Open-loop vs. Closed-loop manoeuvres

The open-loop model G_{LTV} is augmented with an $\mathcal{H}_\infty$ controller designed to suppress the onset of flutter at the open-loop flutter speed and extend the FLEXOP demonstrator valid flight region. A description of the synthesis strategy is provided in [14] in the Section dedicated to the University of Bristol contribution. Briefly, the design process used as performance channels the modal speeds for the first two flexible modes. The controller is a single LTI state-space system with 4 states, 4 inputs (pitch rate q, a_{z-CG}, a_{z-tR}, a_{z-tL}) and 2 outputs (δ_{ail-L4} and δ_{ail-R4}).

For ease of comparison, the previous results from the (open-loop, OL) LTV analysis are repeated in Tab. 3 together with the results from the application of the LTV analysis method to the closed-loop case (CL).

Table 3 Comparison of OL and CL performance

Plant	$\lVert G \rVert_2^{tR}$	$\lVert G \rVert_E^{tR}$	$\lVert G \rVert_2^{CG}$	$\lVert G \rVert_E^{CG}$
OL	20	32	2.7	3.8
CL	4.3	21.2	0.72	1.8

A number of observations can be made with reference to the results in Tab. 3. It is first seen that

21

the controller is able to significantly reduce all the gains. This is pronounced in the induced $\mathcal{L}_2$ gain case, for which it can be noticed also that the gap between $||G||_2^{tR}$ and $||G||_2^{CG}$ is reduced. This was previously described as a measure of the flexibility of the system, and thus the analyses showcase the ability of the controller to tackle it. When looking at the Euclidean gain (third and fifth columns), there is less improvement between OL and CL case, and the gap between $||G||_E^{tR}$ and $||G||_E^{CG}$ has actually increased. Note that this result can be motivated by considering the rationale behind the design technique employed for the investigated controller. It is based on the $\mathcal{H}_\infty$ formalism, which aims at reducing the frequency response peaks of the closed loop and thus is expected to enhance the performance for the induced $\mathcal{L}_2$ gain (as also proved here), and not necessarily for others. In conclusion, the analyses are able to point out performance metrics for which the controller is less effective and can thus inform a redesign if these are deemed important in the tests.

Additional insights are provided by calculating the worst-case disturbance that maximizes the energy of the selected output. Fig. 7 shows a comparison between the open-loop and closed-loop cases for the CG acceleration. A substantial difference is observed in the time-domain profile of the signals. Specifically the CL case has a (dominant) lower frequency of approximatively $10\frac{rad}{s}$, whereas the OL has a frequency of about $50\frac{rad}{s}$, close to that of the two first bending modes [14]. This shows that the controller achieves a reduction in the closed-loop $\mathcal{L}_2$ gain by reducing the energy associated with the first elastic modes (which was indeed the aim of the design process as mentioned before). Indeed, the worst-case gust associated with the CL excites lower frequency modes of the system, which have a lower energy content, thus resulting in the improved gain. It is also interesting to note that in the CL case the disturbance acts on a shorter time window. This is a feature observed also in other tests that were performed comparing the open and closed loops.

Finally, the sensitivity of the shape of the worst-case signal to the length of the finite horizon T is considered. Based on the nominal manoeuvre defined in Sec. V A, its value has been set to $5.3s$ so far. However, off-nominal conditions in the mission might result in a different value (e.g. because of a different covered distance L_{ac}). In order to investigate the effect on the results, the disturbances predicted for the closed loop case for larger horizons lengths (20%, 50%, and 100% larger than the nominal value T_0, respectively) are considered. The results are shown in Fig. 8, where also the
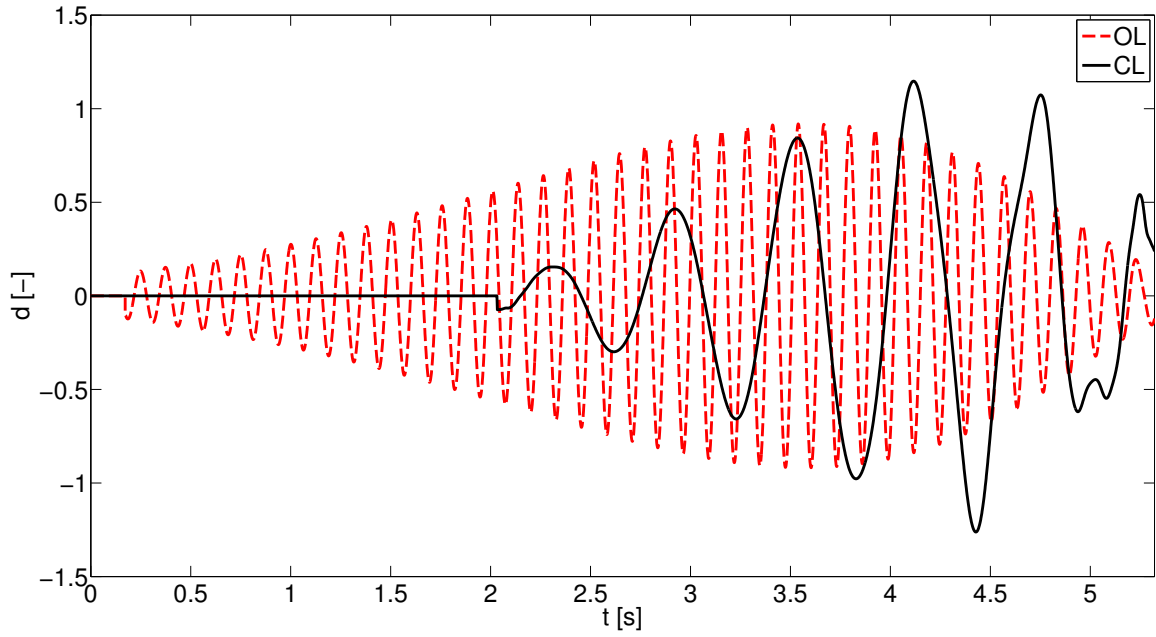
Fig. 7 $\mathcal{L}_2$ **gain worst-case disturbances for** a_{z-CG}: **OL vs CL.**

case of nominal T_0 (corresponding to the curve CL in the previous plot) is reported. For a better comparison, the time t is adimensionalized for each curve with the corresponding horizon length.
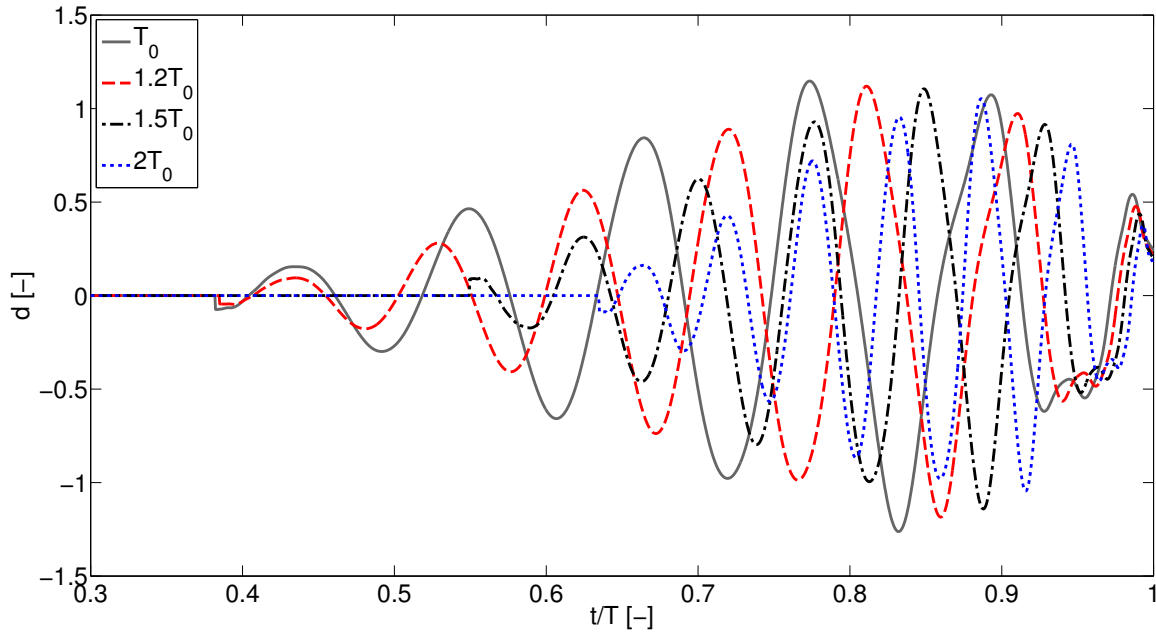

Fig. 8 Effect of T **on the** $\mathcal{L}_2$ **gain worst-case disturbances for the CL system.**

It can be observed that the disturbances are qualitatively very similar. In fact, they present the same dominant frequency and distinctive signal features (e.g. higher frequency component towards

the end of the horizon). Moreover, the $\mathcal{L}_2$ gains corresponding to each curve are within 1.5 % with respect to the performance metric associated with the nominal case (Table 3). It can then be concluded that, for this example, the algorithm is robust to changes in the horizon T. This property, also observed for other analyzed scenarios, is advantageous because the gained insights (as those from Fig. 7) are not limited to specific cases but have a more general validity.

D.   Comparison with standard gust performance analysis

The results obtained with this framework are compared now with those from a standard approach widely used in the aerospace field for gust analysis. Atmospheric turbulence is typically considered for aircraft design purposes in one of the two idealized categories [23, 24]: discrete gusts, where the gust speed varies in a deterministic manner (provided in time domain); continuous turbulence, where the gust velocity is assumed to vary randomly (provided in frequency domain). The former case is considered here, of which the most common example is the so called *1-cosine* gust. This provides the spatial variation of the vertical gust as

$$w_g(x_g) = \frac{w_{g0}}{2}\left(1 - \cos\left(\frac{2\pi x_g}{L_g}\right)\right) \quad 0 \le x_g \le L_g \tag{31}$$

where w_{g0} is the value of the peak gust velocity and L_g is the gust length. For a given energy associated with the gust signal, Eq. (31) describes a set of gusts which vary depending on the gust length L_g. The comparison performed in this subsection is then between the performance achieved when the aircraft is subject to this set of gust profiles and that resulting from the worst-case analyses presented in Sec. V B.

To this aim, the gust velocity expression needs first to be transformed from a spatial into a temporal function. This can be done recalling that the manoeuvre features a constant acceleration, and thus x_g is a quadratic function of time. The temporal signal will then be denoted by d_g. A family of 15 gusts for $\frac{L_{ac}}{15} \le L_g \le L_{ac}$ is computed and plotted in Fig. 9. The signals are normalized and adimensionalized such that $||d_g||_{2,[0,T]}=1$.

This set of gusts is then simulated in the LTV plant G_{LTV} presented in Sec. V B. Fig. 10(a) and Fig. 10(b) report the two performance metrics as a function of the gust length L_g for a_{z-CG} and a_{z-tR} respectively.
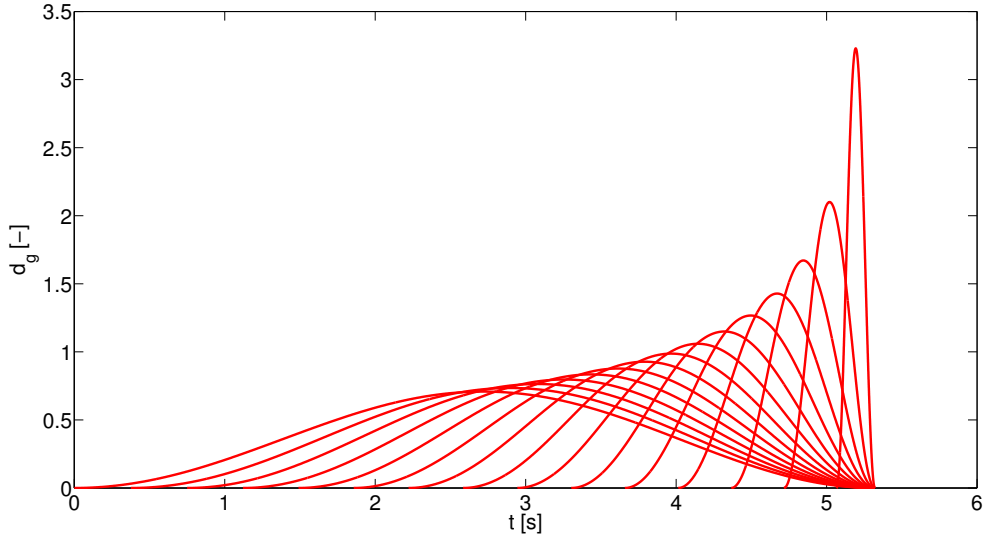
24

Fig. 9 Set of *1-cosine* gust signals for different gust length L_g.
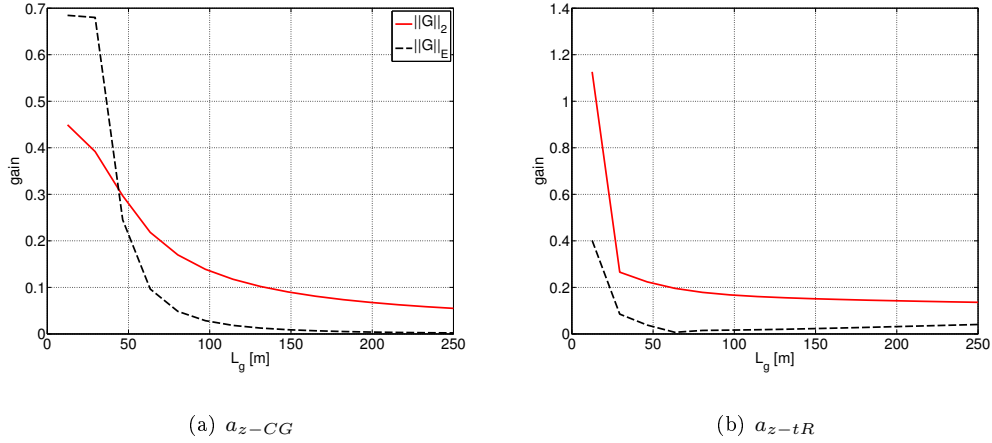

(a) a_{z-CG}

(b) a_{z-tR}

Fig. 10 $\mathcal{L}_2$ and Euclidean gains corresponding to d_g as a function of the gust length L_g.

The performance gains reported in Fig. 10 are markedly different from those in Tab. 2 (*OL* row). These differences are not only quantitative, but also qualitative. For example, it can be noted that for the tip acceleration (Fig. 10(b)) these analyses point out at a larger value for $||G||_2$ than for $||G||_E$, whereas Tab. 2 indicated the opposite.

These differences should be interpreted noting that a mathematical guaranteed worst-case signal is provided by the proposed analysis method (i.e., Algorithm 2). Further, the computed disturbance is a function of the particular performance metric and output considered (examples of this were given in Section V B). In view of this, it is thus expected that the performance associated with the worst-case gust $\bar{d}$ will be worse than other idealized gusts having a given shape which is independent of the

particular performance problem studied (as it is the case for the *1-cosine* gust). Of course, as intrinsic to all worst-case analyses (and especially those based on robust analytical methods), the computed signals do not usually have associated a probability of occurrence. Thus, the usual trade-off between analyzing for cases that are very probable (but that yield *optimistic* results) versus analyzing for a potentially very improbable case (but providing guaranteed worst-case answers) applies in here. In any case, once the gap between the predictions obtained with standard approaches and the actual worst-case is assessed, the proposed framework allows to construct the signal determining such a performance degradation. This knowledge can in turn drive additional investigations focused on specific objectives (e.g. determining the largest wing tip deflections).

Future research can look at more physical worst-case gust disturbances, and attempt to connect them with more elaborate gust models from the literature (e.g. Dryden Wind Turbulence Model). In addition to the gust example proposed here, other applications to the analysis and design of very flexible aircraft are envisaged. For example, the active load alleviation problem, which has been drawing increasing interest in the community [25], can benefit from the developed analysis framework. Indeed, this can be used to identify worst-case manoeuvres which prevent from achieving the performance targets and can in turn inform redesign of the feedback loop.

VI. Conclusions

This paper explores the computation of worst-case disturbances associated with finite horizon LTV systems. The definition of the signal leverages the connection between a quadratic cost function (specifying a performance objective) and a Riccati differential equation. The main technical result of the paper is a numerically reliable algorithm which exploits the solution of the RDE and the structure of the disturbance. The effectiveness of the approach is demonstrated with an example consisting of a flexible aircraft subject to gust. This application exemplifies some of the insights that can be gained with this framework and includes a comparison with a standard approach used for gust analysis. Extensions of this work can focus, from the theoretical side, on adding constraints to the input signal in order to obtain more physical worst-case disturbances (e.g. bounds on the magnitude or rate of d) and, from an application perspective, on investigating other manoeuvres of interest in the analysis of very flexible aircraft.

Appendix A

Lemma 4. *Let $M \in \mathbb{S}^n$ and $v, w \in \mathbb{R}^n$. Then it holds*

$$|v^T M v - w^T M w| \leq \bar{\sigma}(M) \left[||v|| + ||w||\right] ||v - w|| \tag{32}$$

Proof. The symmetry of M implies that $w^T M v = v^T M w$. This can be used to show the following relationship

$$v^T M v - w^T M w = (v - w)^T M(v + w) \tag{33}$$

This leads to the following bound:

$$\begin{aligned}
|v^T M v - w^T M w| &= |(v - w)^T M(v + w)| \\
&\leq ||M(v + w)|| \, ||v - w|| \\
&\leq \bar{\sigma}(M)\left[||v|| + ||w||\right] ||v - w||
\end{aligned} \tag{34}$$

The first inequality follows Eq. (33) and Cauchy-Schwartz inequality. The second inequality follows from the definition of $\bar{\sigma}(M)$. The last inequality is an application of the triangle inequality.

$\square$

References

[1] Tuzcu, I., "On the stability of flexible aircraft," *Aerospace Science and Technology*, Vol. 12, No. 5, 2008, pp. 376 – 384.

[2] Su, W. and Cesnik, E., "Dynamic Response of Highly Flexible Flying Wings," *AIAA Journal*, Vol. 49, No. 2, 2011, pp. 324–339.

[3] Avanzini, G., Nicassio, F., , and Scarselli, G., "Reduced-Order Short-Period Model of Flexible Aircraft," *Journal of Guidance, Control and Dynamics*, Vol. 40, No. 8, 2017, pp. 2017–2029.

[4] Avanzini, G., Capello, E., and Piacenza, I. A., "Mixed Newtonian-Lagrangian Approach for the Analysis of Flexible Aircraft Dynamics," *Journal of Aircraft*, Vol. 51, No. 5, 2014, pp. 1410–1421.

[5] Schmidt, D. K., Zhao, W., and Kapania, R. K., "Flight-Dynamics and Flutter Modeling and Analyses of a Flexible Flying-Wing Drone," AIAA Atmospheric Flight Mechanics Conference, AIAA SciTech Forum, 2016.

[6] Iannelli, A., Marcos, A., and Lowenberg, M., "Study of Flexible Aircraft Body Freedom Flutter with Robustness Tools," *Journal of Guidance, Control, and Dynamics*, Vol. 41, No. 5, 2018, pp. 1083–1094.

[7] Khalil, H. K., *Nonlinear systems*, Prentice Hall, 1996.

[8] Menon, P., Bates, D., and Postlethwaite, I., "Computation of Worst-Case Pilot Inputs for Nonlinear Flight Control System Analysis," *Journal of Guidance, Control and Dynamics*, Vol. 29, No. 1, 2006, pp. 195–199.

[9] Fielding, C., Varga, A., Bennani, S., Selier, M., and Eds., *Advanced Techniques for Clearance of Flight Control Laws*, Springer-Verlag Berlin Heidelberg, 2002.

[10] Green, M. and Limebeer, D., *Linear robust control*, Prentice Hall, 1995.

[11] Seiler, P., Moore, R., Meissen, C., Arcak, M., and Packard, A., "Finite Horizon Robustness Analysis of LTV Systems Using Integral Quadratic Constraints," *Automatica*, Vol. 100, 2019, pp. 135–143.

[12] Dieci, L., Osborne, M. R., and Russell, R. D., "A Riccati Transformation Method for Solving Linear BVPs. II: Computational Aspects," *SIAM Journal on Numerical Analysis*, Vol. 25, No. 5, 1988, pp. 1074–1092.

[13] Cantoni, M. and Sandberg, H., "Computing the L2 gain for linear periodic continuous-time systems," *Automatica*, Vol. 45, No. 3, 2009, pp. 783 – 789.

[14] Luspay, T., Ossmann, D., Wuestenhagen, M., Teubl, D., Baar, T., Peni, T., Pusch, M., Kier, T., Waitman, S., Iannelli, A., Marcos, A., Lowenberg, M., and Vanek, B., "Flight control design for a highly flexible flutter demonstrator ," AIAA SciTech Forum, 2019.

[15] Stahl, P., Sendner, F., Hermanutz, A., Robler, C., and Hornung, H., "Mission and Aircraft Design of FLEXOP Unmanned Flying Demonstrator to Test Flutter Suppression within Visual Line of Sight," 17th AIAA Aviation Technology, Integration, and Operations Conference, 2017.

[16] Murray, R. M., Zexiang, L., and Sastry, S. S., *A Mathematical Introduction to Robotic Manipulation*, CRC Press, Inc., Boca Raton, FL, USA, 1st ed., 1994.

[17] Marcos, A. and Bennani, S., "LPV modeling, analysis and design in space systems: Rationale, objectives and limitations," AIAA Guidance, Navigation, and Control Conference, 2009.

[18] Brockett, R., *Finite dimensional linear systems*, Series in decision and control, Wiley, 1970.

[19] Zhou, K., Doyle, J. C., and Glover, K., *Robust and Optimal Control*, Prentice-Hall, Inc., 1996.

[20] Seiler, P., Buch, J., Moore, R., Meissen, C., Arcak, M., and Packard, A., "LTVTools (Beta), A MATLAB Toolbox for Linear Time-Varying System- https://www.mathworks.com/matlabcentral/fileexchange/69563-ltvtools," 2018.

[21] Hodges, D. H. and Pierce, G. A., *Introduction to Structural Dynamics and Aeroelasticity*, Cambridge University Press, 2011.

[22] Schmidt, D., *Modern flight dynamics*, McGraw-Hill, 2012.

[23] Hoblit, F., *Gust Loads on Aircraft: Concepts and Applications*, AIAA education series, American Institute of Aeronautics & Astronautics, 1988.

[24] Wright, J. and Cooper, J., *Introduction to Aircraft Aeroelasticity and Loads*, AIAA education series, John Wiley & Sons, 2007.

[25] Xu, J. and Kroo, I., "Aircraft Design with Active Load Alleviation and Natural Laminar Flow," *Journal of Aircraft*, Vol. 51, No. 5, 2014, pp. 1532–1545.